Southern Hemisphere extra-tropical gravity wave sources and intermittency revealed by a middle atmosphere General Circulation Model

Simon P. Alexander * Australian Antarctic Division, Hobart, Australia

Kaoru Sato

Department of Earth and Planetary Science, University of Tokyo, Tokyo, Japan

Shingo Watanabe and Yoshio Kawatani

Research Institute for Global Change, Japan Agency for Marine-Earth Science and Technology, Yokohama, Kanagawa, Japan

Damian J. Murphy

Australian Antarctic Division, Hobart, Australia

J. Atmos. Sci., in press.
doi: http://dx.doi.org/10.1175/JAS-D-15-0149.1

* *Corresponding author address:* Simon Alexander, Australian Antarctic Division, 203 Channel Highway, Kingston TAS 7050, Australia.

E-mail: simon.alexander@aad.gov.au

ABSTRACT

Southern Hemisphere extra-tropical gravity wave activity is examined using simulations from a free-running middle atmosphere general circulation model called Kanto which contains no gravity wave parameterizations. The total absolute gravity wave momentum flux (MF) and its intermittency, diagnosed by the Gini coefficient, are examined during January and July. The MF and intermittency results calculated from the Kanto model agree well with results from satellite limb and super-pressure balloon observations. The analysis of the Kanto model simulations indicates the following results. Non-orographic gravity waves are generated in Kanto in the frontal regions of extra-tropical depressions and around tropopause-level jets. Regions with lower (higher) intermittency in the July mid-stratosphere become more (less) intermittent by the mesosphere due to lower-level wave removal. The gravity wave intermittency is low and nearly homogeneous throughout the SH middle atmosphere during January. This indicates that non-orographic waves dominate at this time of year, with sources including continental convection as well as oceanic depressions. Most of the zonal-mean MF at $40° - 65°$S in January and July is due to gravity waves located above the oceans. The zonal-mean MF at lower latitudes in both months has a larger contribution from the land regions but the fraction above the oceans remains larger.

1. Introduction

Despite their relatively small scale, gravity waves are an important component of the atmospheric general circulation because they transfer momentum upward from tropospheric sources to the middle atmosphere. The gravity wave drag generated upon breaking closes the mesospheric jet and induces a summer to winter pole mesospheric circulation (Haynes et al. 1991; Garcia and Boville 1994). Gravity waves, together with planetary waves, drive the winter polar stratosphere away from its radiatively determined state: the existence of the winter polar stratopause itself is an indicator of strong gravity wave forcing (Hitchman et al. 1989). Gravity wave driving contributes to the Quasi-Biennial Oscillation (QBO) (Sato and Dunkerton 1997; Kawatani et al. 2010; Ern et al. 2014). The temperature perturbations of gravity waves can induce the formation and affect the composition of polar stratospheric and polar mesospheric clouds when the background temperature is close to the clouds' formation thresholds (Carslaw et al. 1998; Dörnbrack et al. 2001; Shibata et al. 2003; Höpfner et al. 2006; McDonald et al. 2009; Alexander et al. 2011; Kaifler et al. 2013).

Southern Hemisphere gravity wave sources vary seasonally and latitudinally. Higher gravity wave activity is observed at high southern latitudes during winter than during summer. This enhanced wave activity is due to stronger winter sources such as wave generation by fronts and jets, as well as the generation of waves from orographic sources (Yan et al. 2010; Ern et al. 2011; Alexander and Grimsdell 2013; Hendricks et al. 2014). Conversely, during summer, gravity wave activity increases in the tropical and sub-tropical regions as a result of enhanced deep convective activity and latent heat release above the continents (Jiang et al. 2004; Alexander et al. 2008c). The major sources of Southern Hemisphere orographic gravity waves (OGWs) visible in climatologies are the Andes and Antarctic Peninsula (e.g. Baumgaertner and McDonald (2007); Alexander et al. (2009b); Sato et al. (2012); Geller et al. (2013)). Large OGW activity is often observed to extend significant distances downstream (leeward) from these mountainous regions, indicative of momentum flux deposition occurring significant distances from the OGW sources, and often above oceanic regions (Preusse et al. 2002; Sato et al. 2012). Islands in the Southern Ocean have also been identified as sources of OGWs (Alexander et al. 2009a; Alexander and Grimsdell 2013) as well as mountainous regions in southern Africa and southern Australia (Eckermann and Wu 2012). Katabatic winds draining the interior of Antarctica can excite OGWs as they flow over topographical features (Watanabe et al. 2006; Tomikawa et al. 2015). Synoptic-scale depressions centred over the Southern Ocean direct winds onto the East Antarctic coast where they interact with katabatic winds or ice topography to produce OGWs (Orr et al. 2014; Alexander and Murphy 2015).

Non-orographic gravity wave (NGW) activity is large above the Southern Ocean during winter (Wu and Eckermann 2008; Alexander et al. 2009b; Hendricks et al. 2014). Observations and modelling indicate that high stratospheric NGW activity and momentum flux is associated with spontaneous adjusment processes and jet instability (Plougonven and Zhang 2014; Yasuda et al. 2015a,b). NGWs may also be generated through convective heating associated with frontal activity and deep convection (Fritts and Nastrom 1992; Eckermann and Vincent 1993; Tsuda et al. 1994; Alexander and Pfister 1995). Case studies using the WRF model in the Southern Ocean indicate the role of moisture and convective updrafts in generating gravity waves (Plougonven et al. 2015). Large NGW activity was observed and modelled around the sub-tropical jet (Sato 1994; Kawatani et al. 2004; Alexander et al.

2008b). Individual OGWs in the Southern Hemisphere stratosphere are responsible for the largest momentum fluxes. The NGWs do not produce the 'hot-spot' of activity characteristic of OGW sources, because the NGWs are emitted from sources which vary temporally and spatially. Yet the NGW sources have a lower intermittency (i. e. they occur more frequently) than the large, but less common OGW events (Plougonven et al. 2013; Wright et al. 2013). The lower intermittency of NGWs means that in the zonal mean, NGWs are responsible for a similar, albeit slightly smaller, contribution as OGWs to total momentum flux in the spring mid-stratosphere above Antarctica (Vincent et al. 2007; Hertzog et al. 2008).

General circulation models used for weather forecasting and climate reseach do not resolve the full spectrum of gravity waves due to their relatively coarse horizontal and vertical resolution. This is especially true for climate models, as it is computationally too expensive to run climate simulations at the very high resolution required for spontaneous wave generation. This situation is unlikely to change in the foreseeable future, therefore gravity wave parameterization schemes have been developed to include the effects on the atmosphere of the unresolved waves. Gravity wave parameterizations determine the momentum forcing of the waves on the atmosphere. These parameterizations need to be constrained by observations of momentum flux, which have been made from instruments including satellites (Ern et al. 2004; Alexander et al. 2008a; Wright et al. 2013), super-pressure balloons (Vincent et al. 2007; Hertzog et al. 2008; Plougonven et al. 2013), radars (Vincent and Reid 1983; Sato 1993; Murayama et al. 1994; Sato 1994; Alexander et al. 2008d; Dutta et al. 2008; Sato et al. 2014) and radiosondes (Sato and Dunkerton 1997; Gong et al. 2008; Murphy et al. 2014), although in each case the instruments can only measure part of the gravity wave spectrum. A parameterization of OGWs was sufficient for GCMs including only the troposphere and lower stratosphere. Nowadays, with climate models increasingly more likely to include the whole stratosphere and even the mesosphere, NGWs must also be parameterized in order to correctly represent the structure of the middle atmosphere (Alexander et al. 2010; Morgenstern et al. 2010). Non-orographic gravity waves remain challenging to parameterize in general circulation models due to the complexity of the flow in which they originate (Plougonven and Zhang 2014). NGW parameterization schemes are more complex than OGW parameterizations and are also complicated by the fact that the generation mechanisms of some jet-front NGWs remains unknown except for several idealized situations (Plougonven and Zhang 2014; Yasuda et al. 2015a).

A few high-resolution general circulation models have recently been developed which do not contain gravity wave parameterizations, that is, all waves are spontaneously generated by the model itself (Watanabe et al. 2008; Becker 2009). Such models can be used for comparisons with observations and other models which do contain gravity wave parameterizations (Geller et al. 2013). However, gravity waves with scales around or below the size of the model resolution are likely not properly simulated by these GCMs. Results from the Kanto GCM illustrated the meridional propagation of gravity waves in the middle atmosphere, where waves in the winter hemisphere propagate poleward and upward into the core of the stratospheric polar night jet (Sato et al. 2009). These model results complement recent observational evidence for meridional wave propagation in the summer and winter hemispheres (Ern et al. 2013; Hindley et al. 2015). The monthly Southern Hemisphere gravity wave activity from Kanto shows peaks associated with large mountain ranges and enhancements around the stratospheric jet (Sato et al. 2012).

The aim of this study is to use the Kanto model to examine the spatial and temporal variability of SH stratospheric momentum flux and its intermittency and determine the contribution to total SH momentum flux from oceanic and land regions during a representative summer and winter month. The model data and its analysis is outlined in Section 2. The results of the gravity wave momentum flux sources and intermittency are detailed in Section 3, including zonal means, regional contributions to total momentum flux and composites of non-orographic gravity wave sources. Lastly, a discussion (Section 4) and summary (Section 5) are presented.

2. Data Analysis

We use data output from a free-running T213L256 atmospheric global circulation model (GCM) called Kanto, developed by Watanabe et al. (2008). No gravity wave parameterizations are used in this model, thus all the gravity waves are generated spontaneously. The model time-step is 30 seconds and the horizontal resolution corresponds to a 0.5625° grid. Despite the lack of parameterizations, Kanto obtains realistic middle atmosphere winds and temperature structure, although the 15 month period of the QBO in the model is shorter than in reality (Watanabe et al. 2008; Kawatani et al. 2010). All physical quantities are sampled hourly. Computing the momentum flux directly from the wind perturbations would require saving model output at very high temporal resolution ($\sim$ 5 minutes) in order to perform the desired spectral analysis. As saving the model output at this resolution is not practical, an alternative method must be used to compute momentum flux from this hourly resolution data. We follow the approach described in Geller et al. (2013) to estimate the square of the total absolute gravity wave momentum flux as:

$$
\begin{aligned}
\mathbf{M}^2 &= \left(1 - \frac{f^2}{\hat{\omega}^2}\right)^2 \rho_0^2 [(\overline{u'w'})^2 + (\overline{v'w'})^2] \\
&= \rho_0^2 \overline{w'^2} (\overline{u'^2} + \overline{v'^2}) \left(1 - \frac{f^2}{\hat{\omega}^2}\right)^2 \left(1 + \frac{f^2}{\hat{\omega}^2}\right)^{-1}
\end{aligned}
\tag{1}
$$

where

$$
\frac{f^2}{\hat{\omega}^2} \approx \left(\frac{fg}{N^2 T_0}\right)^2 \frac{\overline{T'^2}}{\overline{w'^2}}
$$

The T_0 and ρ_0 are the background temperature and densities, which are calculated from the large-scale flow. For this analysis, we filter the data to retain components which have a total horizontal wavenumber n of less than six and define this as the background. The primes indicate gravity wave perturbations which we define as waves with $n > 21$, which is the same cut-off as used previously by Sato et al. (2009, 2012).

Gravity wave activity varies through time and in particular, OGWs are known to occur infrequently although they can be of very large magnitudes (Plougonven et al. 2008). In addition to knowledge of the mean values of gravity wave activity over various regions, it is desirable to know whether the wave field is dominated by a few large events (such as for OGWs) or has a more continuous emission (likely for NGWs). This is quantified by diagnosing the intermittency of the gravity wave field. The intermittency may be defined by, for example, the proportion of time that the mean is exceeded (Sato et al. 2012) or the ratio of the 50th to 90th momentum flux percentiles (Hertzog et al. 2008). Here, we follow Plougonven et al. (2013) by using the Gini coefficient to define the intermittency of the gravity wave momentum fluxes. For a series containing M samples, we have for the mth sample a momentum flux of $\mathbf{M} = \mu_m$, calculated via Equation 1. Assuming that the momentum fluxes are sorted into increasing order (with $1 \leqslant m \leqslant M$), the cumulative sum is expressed as $F_m = \sum_{i=1}^{m} \mu_i$. The mean is expressed as $\overline{\mu} = F_M/M$. The intermittency is determined via:

$$I = \frac{\sum_{m=1}^{M-1} (m\overline{\mu} - F_m)}{\sum_{m=1}^{M-1} m\overline{\mu}} \tag{2}$$

The I will vary between 0 (no intermittency, constant series) and 1 (most intermittent). This method has the advantage of using integration so it is less susceptible to sampling; and this method also avoids a somewhat arbitrary choice of limits.

Kanto was run for three model years, with each year having a length of 360 days and each of the twelve months consisting of 30 days. We analyze data from the three Januarys and three Julys to determine the seasonal changes in gravity wave activity and intermittency in the Southern Hemisphere. The January and July output are consistent with the typical seasonal evolution of the general circulation in the middle atmosphere (Watanabe et al. 2008).

3. Results

a. Momentum flux and intermittency

Figure 1 illustrates the January and July zonal-mean total absolute gravity wave momentum flux (MF) and zonal-mean zonal wind in the Southern Hemisphere. The vectors indicate the meridional and vertical wave potential energy flux ($\rho_0\overline{\phi' v'}$, $\rho_0\overline{\phi' w'}$, where ϕ' is the geopotential height perturbation for $n > 21$) which are parallel to the intrinsic group velocity of the gravity waves (see e. g. Kawatani et al. (2009); Sato et al. (2012)). The January zonal-mean zonal winds are westward above the middle stratosphere at all latitudes. The largest MF in the lower stratosphere is located equatorward of 40°S but diminishes rapidly with altitude as the eastward winds weaken and turn westward. In the upper stratosphere, the MF is largest at low latitudes and decreases poleward. Upward propagating waves are evident equatorward of $\sim$ 30°S.

The zonal-mean MF structure in the middle atmosphere is markedly different during July (Figure 1b). At increasingly higher altitudes in the stratosphere, the large lower stratospheric sub-tropical (equatorward of $\sim$ 30°S) MF decreases as zonal wind speeds decrease. The peak MF shifts upward and poleward into the stratospheric polar night jet core. Gravity waves propagate upward and poleward from the sub-tropical jet region and are focused into the core of the polar night jet (Dunkerton 1984; Senf and Achatz 2011). Waves at higher latitudes (around 70°S) propagate nearly vertically through the middle atmosphere.

The 50 hPa horizontal distribution of the January and July mean MF are shown in Figure 2. The January 50 hPa MF distribution generally decreases poleward with slightly larger MF centred above the continents and New Zealand and extending over their surrounding oceans. The slightly larger MF in the sub-tropics above Africa, northern Australia and sub-tropical South America are likely due to gravity waves emitted by large-scale convection and are qualitatively in agreement with observations of gravity waves attributed to convective sources (Jiang et al. 2004; Alexander et al. 2008c; Ern and Preusse 2012). During July, large MF is present above the southern Andes and the Antarctic Peninsula. Over the ocean, the largest mean MF are above the southern Indian Ocean. Small, local peaks in MF are also visible above topography in New Zealand, Eastern Australia, Tasmania and Southern Africa. These localised regions of enhanced gravity wave activity are also seen frequently in satellite observations (Eckermann and Wu 2012; Hendricks et al. 2014).

By upper stratospheric altitudes (as shown by the 1 hPa MF distributions in Figure 3), the MF has decreased in both seasons. The January peak MF is now located to the east (i. e. upwind) of Southern Africa, New Zealand and South America. The peak MF in July at 1 hPa is above the southern Andes, while the second peak is above Southern Ocean, near the maximum zonal wind speeds. The MF has decreased further by 0.1 hPa, in the mesosphere, (Figure 4), although the distributions are broadly similar to those at 1 hPa with largest January MF in the sub-tropics and to the east of the continents; and largest July MF above the Southern Ocean and southern Andes.

Figure 5 shows the intermittency at 50 hPa. Waves produced above all the mountainous regions are highly intermittent in July. Gini coefficients range from about 0.6 above Eastern Australia, southern Africa and New Zealand to ~ 0.8 above the Antarctic Peninsula. The Gini coefficients above the Andes are 0.6 – 0.7. In contrast, the coefficients above the oceans are lower, typically 0.45 – 0.55. The highest intermittency (i. e. Gini coefficient ~ 0.8) at 50 hPa is above the Trans-Antarctic mountains and the Antarctic Peninsula: these regions have lower monthly mean MF compared with lower-latitude mountainous regions (see Figure 2b). Smaller mountain ranges, such as those in New Zealand, Eastern Australia and southern Africa produce a more intermittent spectrum than their immediate surroundings. There is a higher intermittency for waves above the southern Indian ocean than above other ocean areas. The January intermittency, in contrast to July, is nearly uniform across the entire Southern Hemisphere, with Gini coefficients of 0.45 – 0.55 present above land and ocean.

The intermittency in the July mesosphere (0.1 hPa) has changed from that in the mid stratosphere and is shown in Figure 6. The intermittency has become more uniform across the Southern Hemisphere, with increases above the oceans (coefficients of $\sim 0.5 - 0.6$) and decreases above mountains (coefficients of $0.6 - 0.65$) when compared with Figure 5b. The Gini coefficients calculated from the Kanto model are broadly consistent with those obtained from observations (Plougonven et al. 2013; Wright et al. 2013) and will be compared in detail below.

b. Regional contributions to total momentum flux

We divide the Southern Hemisphere domain into several land and oceanic regions, in order to examine the properties of total momentum flux and intermittency of each region separately. The regional boundaries are illustrated in Figure 7. This division into land and oceanic regions provides a convenient proxy for GW source attribution. We follow the Antarctic boundaries of Plougonven et al. (2013) and note that these boundaries are appropriate in Kanto too, given the structure of the MF at various altitudes (Figure 2 – Figure 4) and the wave intermittency (Figure 5). Based on analyses of the location of the sub-tropical jet (e. g. Sato et al. (2000)), we divide the oceans into the Southern Ocean and Temperate Oceans (the latter consisting of the South Atlantic, South Pacific and southern Indian Oceans) at 45°S. Isolated Southern Ocean islands are combined into the Southern Ocean region because Kanto does not resolve the islands sufficiently. A large region above the South Atlantic is included in South America, which allows for the horizontal propagation of OGW wave trains observed and modelled downwind of the Andes (Preusse et al. 2002; Sato et al. 2012). For the same reason, Drake Passage and South Georgia also form part of South America (see Figure 3).

The 50 hPa zonal-mean MF above all land and all oceans are illustrated in Figure 8c and Figure 8d for January and July respectively, along with the total zonal-mean MF. The zonal-mean MF above land and ocean are normalized by the fraction at each latitude which consists of land and ocean, respectively. The total zonal-mean MF from $\sim$ 40°S – 65°S is mainly due to contributions from oceanic regions. Further north, the land regions contribute a larger fraction of total zonal-mean MF, although the contribution from above the ocean is still larger. From 65°S – 70°S, only a small ocean region exists off the coast of West Antarctica (see Figure 7) so in this latitude band, the zonal-mean MF above land is around twice as large as that above the ocean. The peak in MF in July occurs at around 40°S – 50°S and decreases equatorward. The equatorward increase of MF in January is an indication of the presence of non-orographic gravity wave sources such as convection. Both the land and ocean zonal-mean MF are much lower at 0.1 hPa in January (Figure 8a) and July (Figure 8b), but retain similar relative contributions to total zonal MF as at 50 hPa.

The regional mean MF as a function of altitude is illustrated for January and July in Figure 9. The July mean MF at 100 hPa above the temperate oceans is larger than above the Southern Ocean but smaller above about 50 hPa. This is probably due to polarward propagation of waves and partly due to dissipation near the sub-tropical weak wind layer around 50 hPa (see Figure 1b). MF above all regions decrease with altitude, with the rate of decrease similar above land and oceanic regions. The large July mean MF above the Southern Ocean, South America and the Antarctic Peninsula is visible in Figure 9b, while the large January mean MF above land regions is visible in Figure 9a throughout the middle atmosphere.

The vertical profile of the mean intermittency (expressed as the Gini coefficient) in each region is presented in Figure 10. The intermittency is essentially constant with altitude during January for all regions (~ 0.5). In contrast, the intermittency during July varies with altitude and its behavior depends upon the region. For regions with low intermittency (< 0.55) below 30 hPa, the intermittency increases with altitude. The intermittencies above the Antarctic Peninsula, Coastal Antarctica and South America initially increase before decreasing by the 3 hPa pressure level and at 0.1 hPa are comparable with most other regions. The relatively low mean South American intermittency is a result of the large area of this region (see Figure 7).

c. Non-orographic gravity wave sources and propagation

Convective heating associated with extra-tropical depressions and frontal activity are sources of NGWs (Plougonven et al. 2013). To explore the general behaviour of convective NGW sources in Kanto, the July composite 580 hPa root-mean-squared (rms) horizontal wind divergence of oceanic-region depressions is shown in Figure 11a. To form this composite, oceanic-region depressions which have local minimum altitudes in the 850 hPa geopotential surface field of < 1300 m are identified (the composite mean geopotential height is indicated by the black contour lines on Figure 11). The algorithm finds depressions satisfying these criteria at each hourly model time step. The results are not overly sensitive to the choice of these limits. The resulting composite mid-tropospheric (580 hPa) horizontal wind divergence field is maximum above the frontal region, where precipitation is locally maximum. Gravity waves are emitted from the frontal region (coincident with the precipitation extending north of the composite depression's center) rather than from the actual center where precipitation is maximum. This indicates that fronts are the main source of waves associated with depressions in the Kanto model. The divergence field north of the depression has spread out at 200 hPa (Figure 11b) compared with the mid-troposphere, while a local minimum in divergence exists around and to the west of the composite depression's center. Some of the gravity waves generated by these depressions are probably filtered at pressure levels below 200 hPa, while some propagate and interact with jet-emitted waves.

The other source of extra-tropical NGWs are spontaneous adjustment processes and jet instability. We examine a case of two vertical cross-sections of the divergence field through a depression located in the South Atlantic. The wavelike structures evident in Figure 12 provide information about wave properties and source characteristics in Kanto, which is important for a better understanding of the mean distribution of gravity waves. Convergence and divergence with downward tilting phase fronts occur below the jet core and upward tilting phase fronts occur above the jet core (Figure 12b, around 200 hPa at 10°W – 10°E). This phase structure indicates that the jet itself is the source of these waves. Some of these waves can be easily followed upward to 30 hPa. Phase fronts in the latitude cross-section (Figure 12a) are also seen above about 100 hPa, tilting upward and initially equatorward, although toward 30 hPa the divergence field is only large in the strong zonal wind region of the stratospheric polar jet.

The composite of the middle atmosphere momentum flux of the oceanic NGWs produced through upper tropospheric jet mechanisms is investigated by examining it relative to the cores of the sub-tropical jet (STJ, temperate ocean region) at 200 hPa and the polar-front jet (PFJ, Southern Ocean region) at 300 hPa during July. For each model time-step, data are extracted at longitudes where the horizontal wind speed at 200 hPa (STJ) or 300 hPa (PFJ) is locally maximum and exceeds 50 m s^{-1}. The resultant July composites are shown in Figure 13 and allow us to examine wave propagation through the middle atmosphere relative to the location of the jet source. The MF decreases with height most quickly on the equatorward flank of the STJ (Figure 13a; positive relative latitudes) as the gravity waves propagate into a region of decreasing horizontal wind speed in the middle stratosphere. Such structure in the absolute value of MF is consistent with the concept of critical-level removal of gravity waves by the background winds, leaving fewer waves to propagate to successively higher altitudes. In contrast, the MF above the poleward side of the sub-tropical jet decreases less rapidly. The gravity waves from the STJ are directed upward and poleward into the core of the polar stratospheric jet.

Above the Southern Ocean (Figure 13b), the composite of the PFJ indicates an upward motion of gravity waves and their momentum flux into the core of the polar stratospheric jet. The poleward-directed vectors in the lower stratosphere on the equatorward flank of the PFJ (positive relative latitudes) indicate that some of these waves are propagating southward from the STJ. This contrasts with the nearly vertical propagation of waves on the poleward side of the PFJ.

4. Discussion

The horizontal distributions of MF at 50 hPa, 1 hPa and 0.1 hPa calculated from the Kanto model output data (Figures 2 – 4) may be compared with estimates of MF from satellite and super-pressure balloon observations and with models which use gravity wave parameterizations. It is worth emphasising here that the Kanto model data and the satellite observations are sensitive to overlapping but not identical parts of the gravity wave spectrum (i. e. each having its own observational window (Alexander et al. 2010)). Furthermore, differences in satellite data processing algorithms result in different zonal-mean MF (see Figure 1 of Geller et al. (2013) regarding HIRDLS).

Limb-scanning satellites such as CRISTA and HIRDLS provide vertical profiles of temperature along the orbit track. Horizontal wavelengths are estimated from adjacent profiles, although they remain undersampled (Ern et al. 2004; Alexander et al. 2008a). Absolute values of momentum fluxes are then estimated by combining the horizontal and vertical wavelengths with the temperature perturbations of the gravity waves, although these MF are likely biased low due to uncertainties in the horizontal wavelengths (Preusse et al. 2009). Monthly mean MF in the lower stratosphere around 25 km altitude above the southern tip of South America during May and August 2006 was around 5 mPa as measured by HIRDLS (Alexander et al. 2008a, 2010) and SABER (Ern et al. 2011), but about 30 mPa during August 1997 as measured by CRISTA data (Ern et al. 2004). The HIRDLS and SABER results compare favorably with the July Kanto MF at 50 hPa of 4 – 5 mPa (Figure 2b). In the zonal mean, all three satellites show similar features during August with the largest MF centered at 55°S, similar to the zonal-mean MF in July in Figure 1. Ern et al. (2011)

also reported larger January MF above the sub-tropical continents than above the oceans (monthly means of about 1 – 2 mPa above land at 30 km), consistent with the 50 hPa Kanto results in Figure 2a.

Long-duration super-pressure balloons (the Vorcore campaign) were launched in Antarctica during spring 2005, with the last flight terminating in February 2006. These balloons travelled on isopycnic surfaces (equivalent to $\sim$ 18 km altitude) around Antarctica and the Southern Ocean and provide detailed information on gravity wave sources, intermittency and MF (Hertzog et al. 2008). The Vorcore zonal-mean density-weighted momentum fluxes in the direction of wave propagation $\rho_0\overline{u_{\|}'w'}$ were calculated above orographic and non-orographic regions (some areas, like the East Antarctic plateau, were classified as non-orographic due to their flat topography). Hertzog et al. (2008) demonstrated that about two thirds of total zonal-mean MF south of 70°S was present above mountainous areas. On the other hand, between 45°S and 70°S, the vast majority of zonal-mean MF was due to MF located above oceanic regions. This dominance in the zonal mean of MF above the Southern Ocean is also present in Kanto during January and July (Figure 8). Furthermore, the proportion of ocean to land zonal-mean MF in both January and July is similar at 50 hPa and 0.1 hPa. While individual orographic gravity waves have very large MF, their high intermittency and the localised land areas diminish their importance in the zonal mean. The Kanto results extend further north than the Vorcore observations. Equatorward of $\sim$ 40°S, the land regions contribute towards half of the total zonal-mean MF in July at 50 hPa. This is due to the larger MF above the Andes at these latitudes, along with small contributions from other orography countering the weaker MF above the temperate oceans (Figure 2). Both Vorcore and Kanto in January show a general decrease of total zonal-mean MF poleward and the Kanto total zonal-mean MF is similar in magnitude to the Vorcore data.

The Kanto July intermittency (Figure 6 and Figure 10) converges with altitude toward near-uniform values of 0.5 – 0.6 at 0.1 hPa across the SH extra-tropics, with intermittency above orography reducing from the lower stratosphere, but intermittency above the oceans increasing. Such results can be understood readily by considering the intervening filtering of both NGWs and OGWs, as described in detail by Wright et al. (2013). The decreasing zonal wind speeds with altitude in the sub-tropics will remove waves with lower phase speeds resulting in a more intermittent spectrum. Conversely, OGWs will be removed when the background wind is close to zero, reducing the intermittency. While in July the zonal-mean wind speeds are positive throughout the middle atmosphere (Figure 1b), individual wind profiles where the wind direction changes by more than 180° between source and observing height result in OGW removal (e. g. Baumgaertner and McDonald (2007); Alexander et al. (2013)). The intermittency (expressed as the Gini coefficient) above the Antarctic Peninsula and southern Andes during July at 50 hPa is 0.6 – 0.8 and above the oceans it is 0.45 – 0.55 (Figure 5), while the whole SH has Gini coefficients of ~ 0.5 in January. These compare with Gini coefficients of 0.6 – 0.7 above the Antarctic Peninsula reported by Plougonven et al. (2013) from super-pressure balloon observations made during spring. Using three years of HIRDLS data, Wright et al. (2013) showed higher zonal-mean Gini coefficients in winter than in summer in the SH extra-tropics, along with a convergence of the Gini coefficient with increasing altitude (i. e. a less intermittent wave spectrum). The Kanto results of Figure 10 are similar to the HIRDLS observations, although the Kanto Gini coefficients are larger which may be due to longer averaging (across all seasons) in HIRDLS.

The low intermittency reported in the January lower stratosphere (~ 0.5, see Figure 5a) indicates the dominance of non-orographic wave sources. Furthermore, while the phase speeds of orographic gravity waves vary from zero in a time-varying flow (e. g. Chen et al. (2005)), the majority of mountain waves produced during January will encounter their critical levels due to the lower stratospheric wind reversal present at this time. The non-zero January zonal-mean MF above land is largely a result of gravity wave emission from deep convective activity above the mid-latitude and sub-tropical land masses. The zonal-mean MF above the land and ocean regions presented in Figure 8 provide insights into wave sources and propagation in the Kanto model throughout the SH middle atmosphere. Orographic gravity waves may propagate upward above the land through the middle atmosphere during winter until they break at high altitudes. Eastward propagating depressions produce non-stationary non-orographic gravity waves prior to, during and after encountering the Andes (Sato et al. 2012). The July zonal-mean MF above the land is a combination of orographic gravity waves and non-orographic gravity waves from these synoptic depressions. The orography in Kanto is smoothed from that in reality (and several Southern Ocean islands are not resolved by the model), so the MF generated by the Kanto orography is likely underestimated compared with observations. Despite this smoothed orography, gravity wave temperature perturbations above the Andes in the lower stratosphere in Kanto reach 2 – 3 K (not shown), similar to that reported in satellite observations (e. g. Eckermann and Preusse (1999)).

Many global circulation models (GCMs) do not have spontaneous wave generation, rather they use a gravity wave parameterization scheme to produce a realistic middle atmosphere circulation. During summer, GCMs with gravity wave parameterizations have larger MF over Antarctica than those seen in observations and with Kanto (Geller et al. 2013), which tend toward zero MF toward the South Pole. These discrepancies were attributed to the source flux specifications in the parameterization schemes (Geller et al. 2013).

Various source mechanisms for the production of extra-tropical non-orographic gravity waves have been proposed following observations and idealized simulations. Recent superpressure balloon observations and modelling results indicate that convective updrafts connected to frontal systems produce high intrinsic frequency waves above the ocean (Plougonven et al. 2015). Large mid-tropospheric horizontal divergence occurs in Kanto in the frontal zone north of the depression's center (Figure 11a). The absence of horizontal wind divergence above the depression's center, where precipitation maximises, indicates that in Kanto, gravity waves are mainly generated in the frontal zone. The strong tropopause-level jets, which are meteorologically linked to these fronts, are themselves a strong source of gravity waves (Figure 12). Gravity waves generated by the tropopause jets propagate into the stratosphere relatively easily (Figure 12 and Figure 13).

Coherent structures of gravity waves around the tropopause-level jet were evident in Figure 12. Using the Kanto data, we estimate the gravity wave parameters of the wave packet located above the core of the jet in Figure 12a (and using additional information provided by other Kanto data - not shown). The resultant gravity wave parameters are summarised in Table 1. While the zonal phase speed c_x is quite large, the background wind is also large, so that the intrinsic zonal phase speed $\hat{c_x} = 9$ m s^{-1}. The horizontal and vertical wavelengths of this wave are similar to those reported in previous model and observational examples of waves generated around the jet (Guest et al. 2000; Plougonven et al. 2003; Kawatani et al. 2004; Watanabe et al. 2008; Murphy et al. 2014).

The results presented here all consider the total absolute value of momentum flux, rather than the zonal and meridonal momentum fluxes, due to the hourly saved Kanto data resolution. Ideally, $\overline{u'w'}$ and $\overline{v'w'}$ are preferable in that they provide directional information on the gravity wave forcing of the background atmosphere. Models respond to the divergence of the gravity waves' zonal and meridional momentum fluxes through its deposition into the background flow. However, as argued by Geller et al. (2013), important information about the state of the atmosphere can still be deduced by considering these total absolute values and this provides a mechanism for comparing models with observations.

5. Conclusion

The spatial and temporal variability of total momentum flux (MF) in the Southern Hemisphere (SH) extra-tropics was examined using the free-running Kanto GCM. Kanto does not have any gravity wave parameterizations, thus all gravity waves are spontaneously generated by the model itself. The seasonal changes in MF were examined by investigating model output in the representative months of January and July (Watanabe et al. 2008). We examine the absolute value of total momentum flux as described by Geller et al. (2013) and diagnose gravity wave intermittency with the Gini coefficient (Plougonven et al. 2013).

The Kanto model results indicate the presence of large, intermittent (Gini coefficients of $0.6 - 0.8$) MF in the middle atmosphere above orography during July. Large, less intermittent (coefficients < 0.55) MF also occur above the Southern Ocean storm tracks during July. Larger MF is present above land than above the oceans during January throughout the middle atmosphere. The entire SH at 50 hPa has near-uniform Gini coefficients of ~ 0.5 in January, indicating that the dominant wave sources are non-orographic, such as summertime continental convection. The results from the Kanto model are consistent with the magnitude and locations of absolute momentum flux determined from satellite limb and super-pressure balloon observations.

The SH is divided into oceanic and land regions, the latter regions including some seas downwind of major orography. Most of the zonal-mean MF at $40° - 65°$S is due to gravity waves above the oceans. The January mean intermittency in each region remains constant (about 0.50) throughout the middle atmosphere. In July, regions with low intermittency in the mid-stratosphere become more intermittent with altitude. In contrast, regions with high intermittency in the mid-stratosphere (the Antarctic Peninsula, Coastal Antarctic and South America) become less intermittent by the lower mesosphere. Such results can be understood by considering the removal of different types of gravity waves with altitude, resulting in a more homogeneous intermittency in the SH at 0.1 hPa than at 50 hPa.

Fronts are the main source region of non-orographic gravity waves associated with depressions above the extra-tropical SH oceans in Kanto. Gravity waves are primarily emitted from fronts, rather than the actual depression centers where precipitation is maximum. Gravity waves are also emitted around the tropopause-level jets in Kanto. Above the oceans, non-orographic gravity waves from the sub-tropical jet propagate upward and poleward into the core of the polar stratospheric jet during July, while waves from the polar-front jet propagate nearly vertically into the stratosphere.

Acknowledgments.

This research was conducted for project 4025 of the Australian Antarctic program and supported by JSPS KAKENHI grants 25247075 and 26610153. The simulation was performed using the Earth Simulator. We appreciate the helpful insights and comments provided by the anonymous reviewers on an earlier version of this manuscript.

REFERENCES

Alexander, M. J., S. D. Eckermann, D. Broutman, and J. Ma, 2009a: Momentum flux estimates for South Georgia island mountain waves in the stratosphere observed via satellite. *Geophys. Res. Lett.*, **36**, L12816, doi:10.1029/2009GL038587.

Alexander, M. J. and A. W. Grimsdell, 2013: Seasonal cycle of orographic gravity wave occurrence above small islands in the Southern Hemisphere: Implications for effects on the general circulation. *J. Geophys. Res.*, **118**, 11 589–11 599, doi:10.10002/2013JD020526.

Alexander, M. J. and L. Pfister, 1995: Gravity wave momentum flux in the lower stratosphere over convection. *Geophys. Res. Lett.*, **22 (15)**, 2029–2032.

Alexander, M. J., et al., 2008a: Global estimates of gravity wave momentum flux from High Resolution Dynamics Limb Sounder observations. *J. Geophys. Res.*, **113**, D15S18, doi:10.1029/2007JD008807.

Alexander, M. J., et al., 2010: Recent developments in gravity-wave effects in climate models and the global distribution of gravity-wave momentum flux from observations and models. *Q. J. R. Meteorol. Soc.*, **136**, doi:10.1002/qj.637.

Alexander, S. P., A. R. Klekociuk, A. J. McDonald, and M. C. Pitts, 2013: Quantifying the role of orographic gravity waves on polar stratospheric cloud occurrence in the Antarctic and the Arctic. *J. Geophys. Res.*, **118**, 11,493–11,507, doi:10.1002/2013JD020122.

Alexander, S. P., A. R. Klekociuk, M. C. Pitts, A. J. McDonald, and A. Arevalo-Torres, 2011: The effect of orographic gravity waves on Antarctic polar stratospheric cloud occurrence and composition. *J. Geophys. Res.*, **116**, D06109, doi:10.1029/2010JD015184.

Alexander, S. P., A. R. Klekociuk, and T. Tsuda, 2009b: Gravity wave and orographic wave activity observed around the Antarctic and Arctic stratospheric vortices by the COSMIC GPS-RO satellite constellation. *J. Geophys. Res.*, **114**, D17103, doi:10.1029/2009JD011851.

Alexander, S. P. and D. J. Murphy, 2015: The seasonal cycle of lower-tropospheric gravity wave activity at Davis, Antarctica (69°S, 78°E). *J. Atmos. Sci.*, **72**, 1010–1021, doi:10.1175/JAS-D-14-0171.1.

Alexander, S. P., T. Tsuda, and Y. Kawatani, 2008b: COSMIC GPS Observations of Northern Hemisphere winter stratospheric gravity waves and comparisons with an atmospheric general circulation model. *Geophys. Res. Lett.*, **35**, L10808, doi:10.1029/2008GL033174.

Alexander, S. P., T. Tsuda, Y. Kawatani, and M. Takahashi, 2008c: Global distribution of atmospheric waves in the equatorial upper troposphere and lower stratosphere: COSMIC observations of wave mean flow interactions. *J. Geophys. Res.*, **113**, D24115, doi:10.1029/2008JD010039.

Alexander, S. P., T. Tsuda, Y. Shibagaki, and T. Kozu, 2008d: Seasonal gravity wave activity observed with the Equatorial Atmosphere Radar and its relation to rainfall information from the Tropical Rainfall Measuring Mission. *J. Geophys. Res.*, **113**, D02104, doi:10.1029/2007JD008777.

Baumgaertner, A. J. G. and A. J. McDonald, 2007: A gravity wave climatology for Antarctica compiled from Challenging Minisatellite Payload / Global Positioning System (CHAMP/GPS) radio occultations. *J. Geophys. Res.*, **112**, D05103, doi:10.1029/2006JD007504.

Becker, E., 2009: Sensitivity of the upper mesosphere to the Lorenz energy cycle of the troposphere. *J. Atmos. Sci.*, **66**, 647–666, doi:10.1175/2008JAS2735.1.

Carslaw, K. S., et al., 1998: Particle microphysics and chemistry in remotely observed mountain polar stratospheric clouds. *J. Geophys. Res.*, **103 (D5)**, 5785–5796.

Chen, C. C., D. R. Durran, and G. J. Hakim, 2005: Mountain-wave momentum flux in an evolving synoptic-scale flow. *J. Atmos. Sci.*, **62**, 3213–3231.

Dörnbrack, A., M. Leutbecher, J. Reichardt, A. Behrendt, K.-P. Müller, and G. Baumgarten, 2001: Relevance of mountain wave cooling for the formation of polar stratospheric clouds over Scandinavia: Mesoscale dynamics and observations for January 1997. *J. Geophys. Res.*, **106 (D2)**, 1569–1581.

Dunkerton, T. J., 1984: Inertia-gravity waves in the stratosphere. *J. Atmos. Sci.*, **41**, 3396–3404.

Dutta, G., T. Tsuda, P. V. Kumar, M. C. A. Kumar, S. P. Alexander, and T. Kozu, 2008: Seasonal variation of short-period (< 2h) gravity wave activity over Gadanki, India (13.5°N,79.2°E). *J. Geophys. Res.*, **113**, D14103, doi:10.1029/2007JD009178.

Eckermann, S. D. and P. Preusse, 1999: Global Measurements of Stratospheric Mountain Waves from Space. *Science*, **286**, 1534–1537.

Eckermann, S. D. and R. A. Vincent, 1993: VHF radar observations of gravity-wave production by cold fronts over Southern Australia. *J. Atmos. Sci.*, **50 (6)**, 785–806.

Eckermann, S. D. and D. L. Wu, 2012: Satellite detection of orographic gravity-wave activity in the winter subtropical stratosphere over Australia and Africa. *Geophys. Res. Lett.*, **39**, L21807, doi:10.1029/2012GL053791.

Ern, M. and P. Preusse, 2012: Gravity wave momentum flux spectra observed from satellite in the summertime subtropics: Implications for global modeling. *Geophys. Res. Lett.*, **39**, L15810, doi:10.1029/GL052659.

Ern, M., P. Preusse, M. J. Alexander, and C. D. Warner, 2004: Absolute values of gravity wave momentum flux derived from satellite data. *J. Geophys. Res.*, **109**, D20103, doi: 10.1029/2004JD004752.

Ern, M., P. Preusse, J. C. Gille, C. L. Hepplewhite, M. G. Mlynczak, J. M. Russell III, and M. Riese, 2011: Implications for atmospheric dynamics derived from global observations of gravity wave momentum flux in stratosphere and mesosphere. *J. Geophys. Res.*, **116**, D19107, doi:10.1029/2011JD015821.

Ern, M., P. Preusse, S. Kalisch, M. Kaufmann, and M. Riese, 2013: Role of gravity waves in the forcing of quasi two-day waves in the mesosphere: An observational study. *J. Geophys. Res.*, **118**, 3467–3485, doi:10.1029/JD018208.

Ern, M., et al., 2014: Interaction of gravity waves with the QBO: A satellite perspective. *J. Geophys. Res.*, **119**, 2329–2355, doi:10.1002/2013JD020731.

Fritts, D. C. and G. D. Nastrom, 1992: Sources of mesoscale variability of gravity waves. Part II: Frontal, convective and jet stream excitation. *J. Atmos. Sci.*, 111–127.

Garcia, R. R. and B. A. Boville, 1994: "Downward Control" of the mean meridional circulation and temperature distribution of the polar winter stratosphere. *J. Atmos. Sci.*, **51**, 2238–2245.

Geller, M. A., et al., 2013: A comparison between gravity wave momentum fluxes in observations and climate models. *J. Climate*, **26**, 6383–6405.

Gong, J., M. A. Geller, and L. Wang, 2008: Source spectra information derived from US high-resolution radiosonde data. *J. Geophys. Res.*, **113**, D10106, doi:10.1029/2007JD009252.

Guest, F. M., M. J. Reeder, C. J. Marks, and D. J. Karoly, 2000: Inertia-Gravity waves observed in the lower stratosphere over Macquarie Island. *J. Atmos. Sci.*, **57**, 737–752.

Haynes, P. H., C. J. Marks, M. E. McIntyre, T. G. Shepherd, and K. P. Shine, 1991: On the "Downward Control" of extratropical diabatic circulations by eddy induced mean zonal forces. *J. Atmos. Sci.*, **48**, 651–678.

Hendricks, E. A., J. D. Doyle, S. D. Eckermann, Q. Jiang, and P. A. Reinecke, 2014: What is the source of the stratospheric gravity wave belt in austral winter? *J. Atmos. Sci.*, **71**, 1583–1592, doi:10.1175/JAS-D-13-0332.1.

Hertzog, A., G. Boccara, R. A. Vincent, F. Vial, and P. Cocquerez, 2008: Estimation of gravity wave momentum flux and phase speeds from quasi-Lagrangian stratospheric balloon flights. Part II: Results from the Vorcore campaign in Antarctica. *J. Atmos. Sci.*, **65**, 3056–3070.

Hindley, N. P., C. J. Wright, N. D. Smith, and N. J. Mitchell, 2015: The southern stratospheric gravity-wave hot spot: Individual waves and their momentum fluxes measured by COSMIC GPS-RO. *Atmos. Chem. Phys.*, **15**, 7797–7818, doi:10.5194/acp-15-7797-2015.

Hitchman, M. H., J. C. Gille, C. D. Rodgers, and G. Brasseur, 1989: The separated polar winter stratopause: A gravity wave driven climatological feature. *J. Atmos. Sci.*, **46**, 410–422.

Höpfner, M., et al., 2006: MIPAS detects Antarctic stratospheric belt of NAT PSCs caused by mountain waves. *Atmos. Chem. Phys.*, **6**, 1221–1230.

Jiang, J. H., B. Wang, K. Goya, K. Hocke, S. D. Eckermann, J. Ma, D. L. Wu, and W. G. Read, 2004: Geographical distribution and interseasonal variability of tropical deep convection: UARS MLS observations and analyses. *J. Geophys. Res.*, **109**, D03111, doi:10.1029/2003JD003756.

Kaifler, N., G. Baumgarten, A. R. Klekociuk, S. P. Alexander, J. Fiedler, and F. J. Lübken, 2013: Small scale structures of NLC observed by lidar at 69°N / 69°S and their possible relation to gravity waves. *J. Atmos. Sol. Terr. Phys.*, **104**, 244–252, doi:10.1016/j.jastp.2013.01.004.

Kawatani, Y., K. Sato, T. J. Dunkerton, S. Watanabe, S. Miyahara, and M. Takahashi, 2010: The roles of equatorial trapped waves and three-dimensionally propagating gravity waves in driving the Quasi-biennial Oscillation. Part I: Zonal mean wave forcing. *J. Atmos. Sci.*, **67**, 963–980, doi:10.1175/2009JAS3222.1.

Kawatani, Y., M. Takahashi, K. Sato, S. P. Alexander, and T. Tsuda, 2009: Global distribution of atmospheric waves in the equatorial upper troposphere and lower stratosphere: AGCM simulation of sources and propagation. *J. Geophys. Res.*, **114**, D01102, doi:10.1029/2008JD010374.

Kawatani, Y., M. Takahashi, and T. Tokioka, 2004: Gravity waves around the subtropical jet of the southern winter in an atmospheric general circulation model. *Geophys. Res. Lett.*, **31**, L22109, doi:10.1029/2004GL020794.

McDonald, A. J., S. E. George, and R. M. Woollands, 2009: Can gravity waves significantly impact PSC occurrence in the Antarctic? *Atmos. Chem. Phys.*, **9**, 8825–8840.

Morgenstern, O. et al., 2010: Review of the formulation of present-generation stratospheric chemistry-climate models and associated external forcings. *J. Geophys. Res.*, **115**, D00M02, doi:10.1029/2009JD013728.

Murayama, Y., T. Tsuda, and S. Fukao, 1994: Seasonal variation of gravity wave activity in the lower atmosphere observed with the MU radar. *J. Geophys. Res.*, **99 (D11)**, 23,057–23,069.

Murphy, D. J., S. P. Alexander, A. R. Klekociuk, P. T. Love, and R. A. Vincent, 2014: Radiosonde observations of gravity waves in the lower stratosphere over Davis, Antarctica. *J. Geophys. Res.*, **119**, 11,973–11,996, doi:10.1002/2014JD022448.

Orr, A., R. Phillips, S. Webster, A. Elvidge, M. Weeks, J. S. Hosking, and J. Turner, 2014: Met Office Unified Model high resolution simulations of a strong wind event in Antarctica. *Q. J. R. Meteorol. Soc.*, doi:10.1002/qj.2296.

Plougonven, R., A. Hertzog, and M. J. Alexander, 2015: Case studies of non-orographic gravity waves over the Southern Ocean emphasize the role of moisture. *J. Geophys. Res.*, **120**, 1278–1299, doi:10.1002/2014JD022332.

Plougonven, R., A. Hertzog, and L. Guez, 2013: Gravity waves over Antarctica and the Southern Ocean: consistent momentum fluxes in mesoscale simulations and stratospheric balloon observations. *Q. J. R. Meteorol. Soc.*, **139**, 101–118, doi:10.1002/qj.1965.

Plougonven, R., A. Hertzog, and H. Teitelbaum, 2008: Observations and simulations of a large amplitude mountain wave breaking over the Antarctic Peninsula. *J. Geophys. Res.*, **113**, D16113, doi:10.1029/2007JD009739.

Plougonven, R., H. Teitelbaum, and V. Zeitlin, 2003: Inertia gravity wave generation by the tropospheric midlatitude jet as given by the Fronts and Atlantic Storm Track Experiment radio soundings. *J. Geophys. Res.*, **108 (D21)**, 4686, doi:10.1029/2003JD003535.

Plougonven, R. and F. Zhang, 2014: Internal gravity waves from atmospheric jets and fronts. *Rev. Geophys.*, **52**, 33–76, doi:10.002/2012RG000419.

Preusse, P., A. Dörnbrack, S. D. Eckermann, M. Riese, B. Schaeler, J. T. Bacmeister, D. Broutman, and K. U. Grossmann, 2002: Space-based measurements of stratospheric mountain waves by CRISTA 1. Sensitivity, analysis method and a case study. *J. Geophys. Res.*, **107 (D23)**, 8178, doi:10.1029/2001JD000699.

Preusse, P. et al., 2009: New perspectives on gravity wave remote sensing by spaceborne infrared limb imaging. *Atmos. Meas. Tech.*, **2**, 299–311.

Sato, K., 1993: Small-scale wind disturbances in the troposphere and lower stratosphere observed by the MU radar during the passage of Typhoon Kelly. *J. Atmos. Sci.*, **50**, 518–538.

Sato, K., 1994: A statistical study of the structure, saturation and sources of inertio-gravity waves in the lower stratosphere observed with the MU radar. *J. Atmos. Terr. Phys.*, **56**, 755–774.

Sato, K. and T. J. Dunkerton, 1997: Estimates of momentum flux associated with equatorial Kelvin and gravity waves. *J. Geophys. Res.*, **102 (D22)**, 26 247–26 261.

Sato, K., S. Tateno, S. Watanabe, and Y. Kawatani, 2012: Gravity wave characteristics in the Southern Hemisphere revealed by a high-resolution middle-atmosphere general circulation model. *J. Atmos. Sci.*, **69**, 1378–1396, doi:10.1175/JAS-D-11-0101.1.

Sato, K., S. Watanabe, Y. Kawatani, Y. Tomikawa, K. Miyazaki, and M. Takahashi, 2009: On the origins of mesospheric gravity waves. *Geophys. Res. Lett.*, **36**, L19801, doi:10.1029/2009GL039908.

Sato, K., K. Yamada, and I. Hirota, 2000: Global characteristics of medium-scale tropopausal waves observed in ECMWF operational data. *Mon. Wea. Rev.*, **128**, 3808–3823.

Sato, K., et al., 2014: Program of the Antarctic Syowa MST/IS radar (PANSY). *J. Atmos. Sol. Terr. Phys.*, **118**, 2–15, doi:10.1016/j.jastp.2013.08.022.

Senf, F. and U. Achatz, 2011: On the impact of middle-atmosphere thermal tides on the propagation and dissipation of gravity waves. *J. Geophys. Res.*, **116**, D241100, doi:10,1029/2011JD015794.

Shibata, T., K. Sato, H. Kobayashi, M. Yabuki, and M. Shiobara, 2003: Antarctic polar stratospheric clouds under temperature perturbation by nonorographic inertia gravity waves observed by micropulse lidar at Syowa Station. *J. Geophys. Res.*, **108 (D3)**, 4105, doi:10.1029/2002JD002713.

Tomikawa, Y., et al., 2015: Vertical wind disturbances during a strong wind event observed by the PANSY radar at Syowa Station, Antarctica. *Mon. Wea. Rev.*, **143**, 1804–1829, doi:10.1175/MWR-D-14-00298.1.

Tsuda, T., Y. Murayama, H. Wiryosumarto, S. W. B. Harijono, and S. Kato, 1994: Radiosonde observations of equatorial atmosphere dynamics over Indonesia 2. Characteristics of gravity waves. *J. Geophys. Res.*, **99 (D5)**, 10 507–10 516.

Vincent, R. A., A. Hertzog, G. Boccara, and F. Vial, 2007: Quasi-Lagrangian superpressure balloon measurements of gravity wave momentum fluxes in the polar stratosphere of both hemispheres. *Geophys. Res. Lett.*, **34**, L19804, doi:10.1029/2007GL031072.

Vincent, R. A. and I. M. Reid, 1983: HF Doppler measurements of mesospheric gravity wave momentum fluxes. *J. Atmos. Sci.*, **40**, 1321–1333.

Watanabe, S., Y. Kawatani, Y. Tomikawa, K. Miyazaki, M. Takahashi, and K. Sato, 2008: General aspects of a T213L256 middle atmosphere general circulation model. *J. Geophys. Res.*, **113**, D12110, doi:10.1029/2008JD010026.

Watanabe, S., K. Sato, and M. Takahashi, 2006: A general circulation model study of the orographic gravity waves over Antarctica excited by katabatic winds. *J. Geophys. Res.*, **111**, D18104, doi:10.1029/2005JD006851.

Wright, C. J., S. M. Osprey, and J. C. Gille, 2013: Global observations of gravity wave intermittency and its impact on the observed momentum flux morphology. *J. Geophys. Res.*, **118**, 10,980–10,993, doi:10.1002/jgrd50869.

Wu, D. L. and S. D. Eckermann, 2008: Global gravity wave variances from Aura MLS: Characteristics and interpretation. *J. Atmos. Sci.*, **65**, 3695–3718, doi:10.1175/2008JAS2489.1.

Yan, X., N. Arnold, and J. Remedios, 2010: Global observations of gravity waves from High Resolution Dynamics Limb Sounder temperature measurements: A yearlong record of temperature amplitude and vertical wavelength. *J. Geophys. Res.*, **115**, D10113, doi:10.1029/2008JD011511.

Yasuda, Y., K. Sato, and N. Sugimoto, 2015a: A theoretical study on the spontaneous radiation of inertia-gravity waves using the renormalization group method. Part I: Derivation of the renormalization group equations. *J. Atmos. Sci.*, **72**, 957–983, doi:10.1175/JAS-D-13-0370.1.

Yasuda, Y., K. Sato, and N. Sugimoto, 2015b: A theoretical study on the spontaneous radiation of inertia-gravity waves using the renormalization group method. Part II: Verification of the theoretical equations by numerical simulation. *J. Atmos. Sci.*, **72**, 984–1009, doi:10.1175/JAS-D-14-0171.1.

List of Tables

1 Gravity wave parameters for the wave present above the jet in Figure 12a. The $\overline{u}$ and N are calculated over the region 20°W – 10°W, 37°S – 47°S and 50 – 100 hPa. 34

TABLE 1. Gravity wave parameters for the wave present above the jet in Figure 12a. The $\overline{u}$ and N are calculated over the region 20°W – 10°W, 37°S – 47°S and 50 – 100 hPa.

λ_x (km)	λ_z (km)	$\lvert f/\hat{\omega} \rvert$	c_x (m s^{-1})	$\hat{c_x}$ (m s^{-1})	$\overline{u}$ (m s^{-1})	N (s^{-1})
1000	3.5	0.3	52	9	43	0.014

List of Figures

1 The zonal-mean MF (color contours) and zonal-mean zonal wind (line contours, units of m s^{-1}, dashed lines indicate westward winds) for (a) January and (b) July. Vectors indicate the meridional and vertical wave potential energy flux ($\rho_0\overline{\phi' v'}$, $\rho_0\overline{\phi' w'}$). Vector lengths are constant between sub-panels with the magnitude given by the horizontal vector in the middle (units of kg m^{-1} s^{-2}). The $\rho_0\overline{\phi' w'}$ are multiplied by a factor of 20 for clarity. The horizontal gray lines in each panel indicate 50 hPa. 38

2 The mean MF (color) and zonal wind (black lines, units of m s^{-1}, westward dashed) at 50 hPa for (a) January and (b) July. The July MF above the Andes reach 20 mPa but the contour scale is clipped at 10 mPa to resolve details above other regions. 39

3 As for Figure 2 but at 1 hPa. 40

4 As for Figure 2 but at 0.1 hPa. 41

5 The intermittency of the absolute momentum fluxes, expressed as the Gini coefficient, at 50 hPa for (a) January and (b) July. Mean zonal wind speeds are also indicated (westward dashed, units m s^{-1}). 42

6 The same as Figure 5 but for the 0.1 hPa intermittency during July. 43

7 Regional boundaries for the decomposition of the Southern Hemisphere extratropics into oceanic and land-based regions. The Indian, South Pacific and South Atlantic oceans north of 45° are combined into one Temperate Ocean region. Grey shading indicates regions classified as oceanic regions, while white indicates land regions. 44

8 January and July zonal-mean MF for the land (dashed) and oceanic (thin solid) regions at (a,b) 0.1 hPa and (c,d) 50 hPa. The thick solid line is the total MF. Note the different scales between the 50 hPa and 0.1 hPa pressure levels. 45

9 Mean MF as a function of pressure level for each region for (a) January and (b) July. Solid lines indicate oceanic regions, while dashed lines indicate land regions. 46

10 Mean intermittency (as measured by the Gini coefficient) as a function of pressure level for each region for (a) January and (b) July. Solid lines indicate oceanic regions, while dashed lines indicate land regions. 47

11 (a) The July mean 580 hPa root mean square horizontal wind divergence (color contours) relative to the center of deep depressions above the ocean, along with the precipitation (white lines, mm day^{-1}), 850 hPa potential temperature in Kelvin (brown lines) and 850 hPa geopotential height in meters (black lines). (b) The same except showing the July mean 200 hPa root mean square horizontal wind divergence (color contours). 48

12 Cross-sections in the South Atlantic of the horizontal wind divergence (color) and zonal wind (black lines, units of m s^{-1}) through the center of a depression at (a) 15°W and (b) 50°S. Vertical gray lines indicate the cross-section for each other's panel. 49

13 July composite MF (color contours) and zonal wind (m s^{-1}, grey lines) for (a) STJ in the temperate oceans and (b) PFJ in the Southern Ocean. Vectors indicate the meridional and vertical wave potential energy flux ($\rho_0\overline{\phi' v'}$, $\rho_0\overline{\phi' w'}$). Vector lengths are constant between sub-panels with the magnitude given by the horizontal vector in the middle (units of kg m^{-1} s^{-2}). The $\rho_0\overline{\phi' w'}$ are multiplied by a factor of 20 for clarity. 50

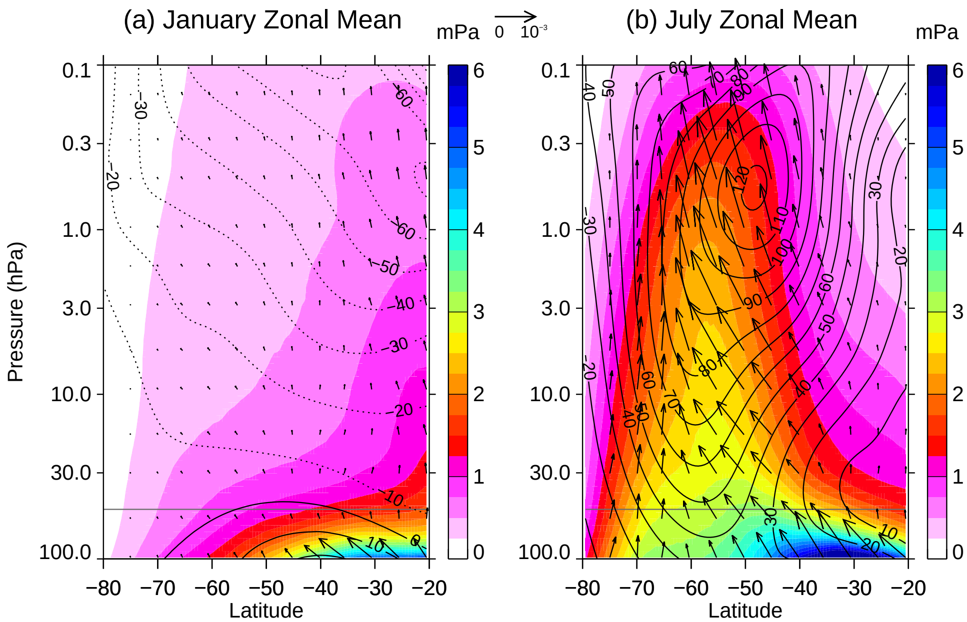

FIG. 1. The zonal-mean MF (color contours) and zonal-mean zonal wind (line contours, units of m s^{-1}, dashed lines indicate westward winds) for (a) January and (b) July. Vectors indicate the meridional and vertical wave potential energy flux ($\rho_0\overline{\phi' v'}$, $\rho_0\overline{\phi' w'}$). Vector lengths are constant between sub-panels with the magnitude given by the horizontal vector in the middle (units of kg m^{-1} s^{-2}). The $\rho_0\overline{\phi' w'}$ are multiplied by a factor of 20 for clarity. The horizontal gray lines in each panel indicate 50 hPa.

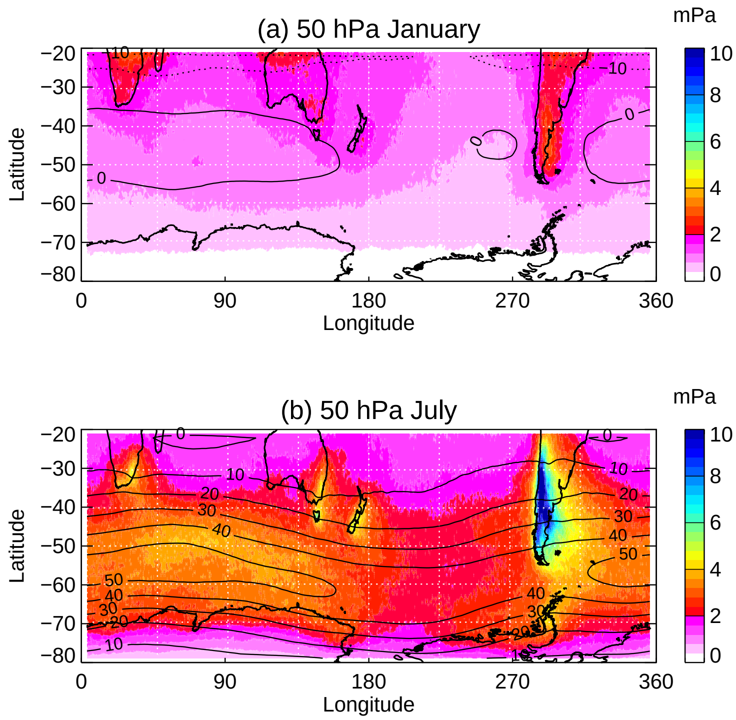

FIG. 2. The mean MF (color) and zonal wind (black lines, units of m s^{-1}, westward dashed) at 50 hPa for (a) January and (b) July. The July MF above the Andes reach 20 mPa but the contour scale is clipped at 10 mPa to resolve details above other regions.

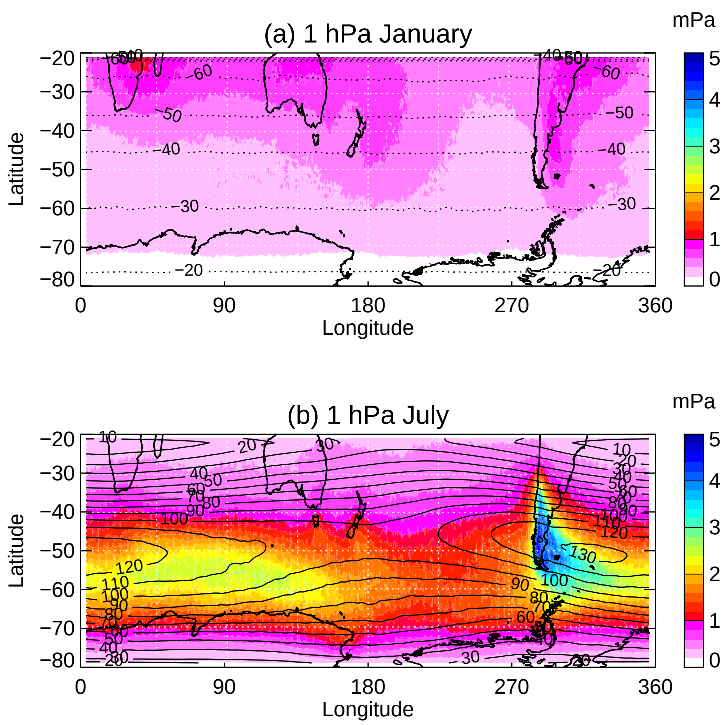

FIG. 3. As for Figure 2 but at 1 hPa.

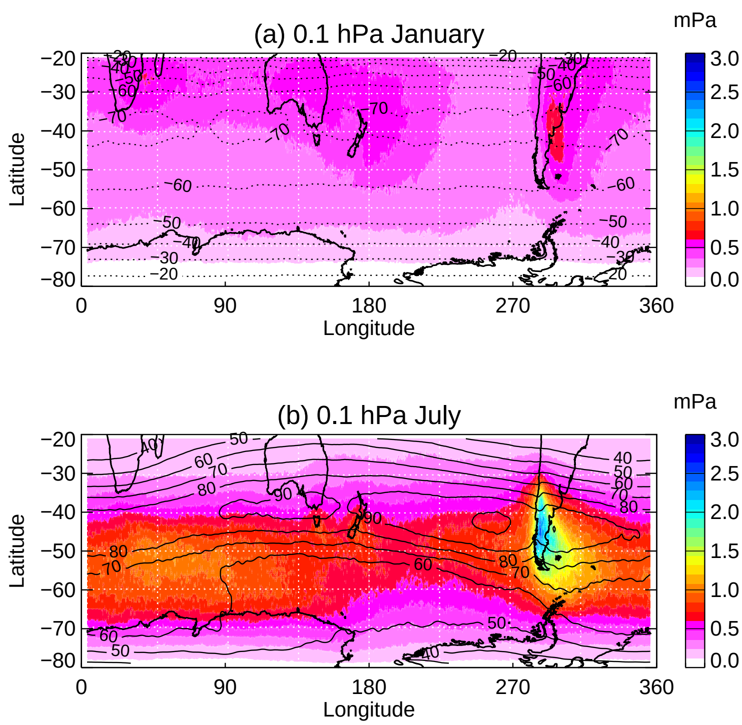

FIG. 4. As for Figure 2 but at 0.1 hPa.

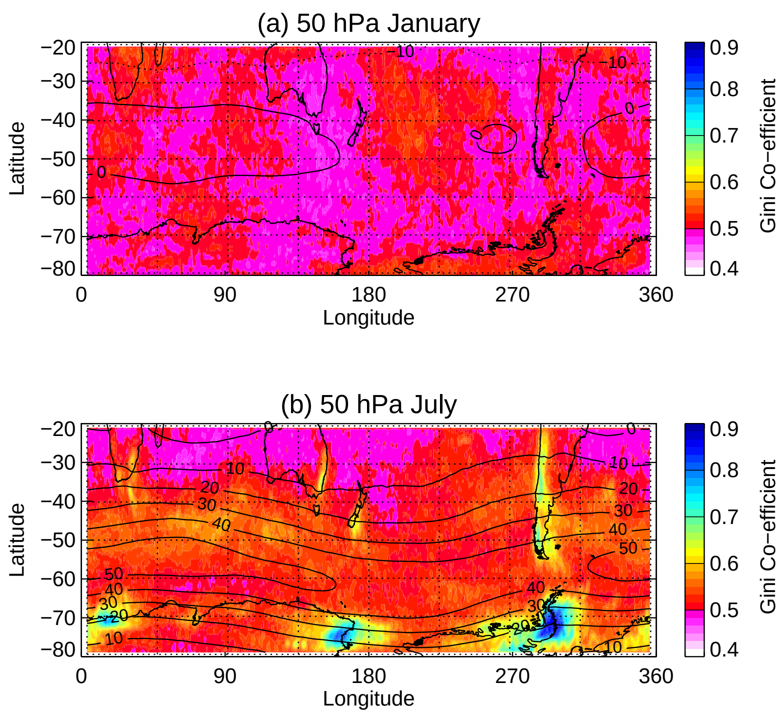

FIG. 5. The intermittency of the absolute momentum fluxes, expressed as the Gini coefficient, at 50 hPa for (a) January and (b) July. Mean zonal wind speeds are also indicated (westward dashed, units m s^{-1}).

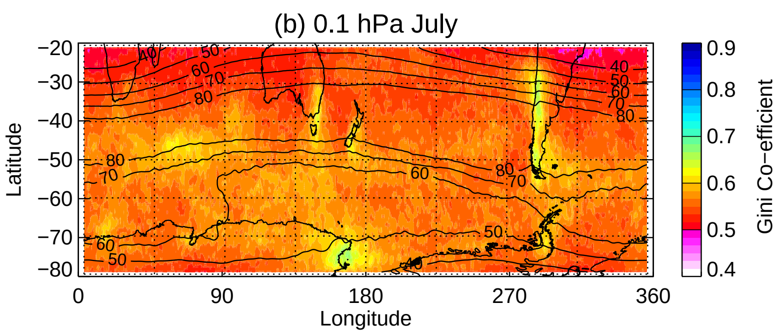

Fig. 6. The same as Figure 5 but for the 0.1 hPa intermittency during July.

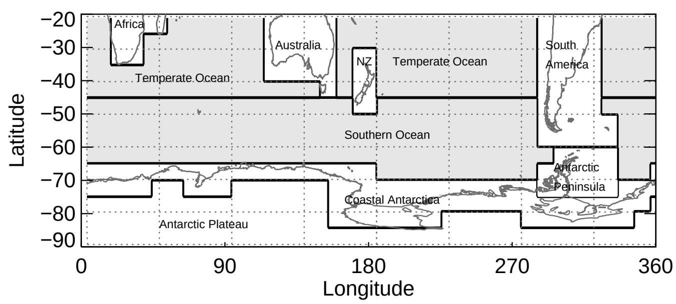

FIG. 7. Regional boundaries for the decomposition of the Southern Hemisphere extra-tropics into oceanic and land-based regions. The Indian, South Pacific and South Atlantic oceans north of 45° are combined into one Temperate Ocean region. Grey shading indicates regions classified as oceanic regions, while white indicates land regions.

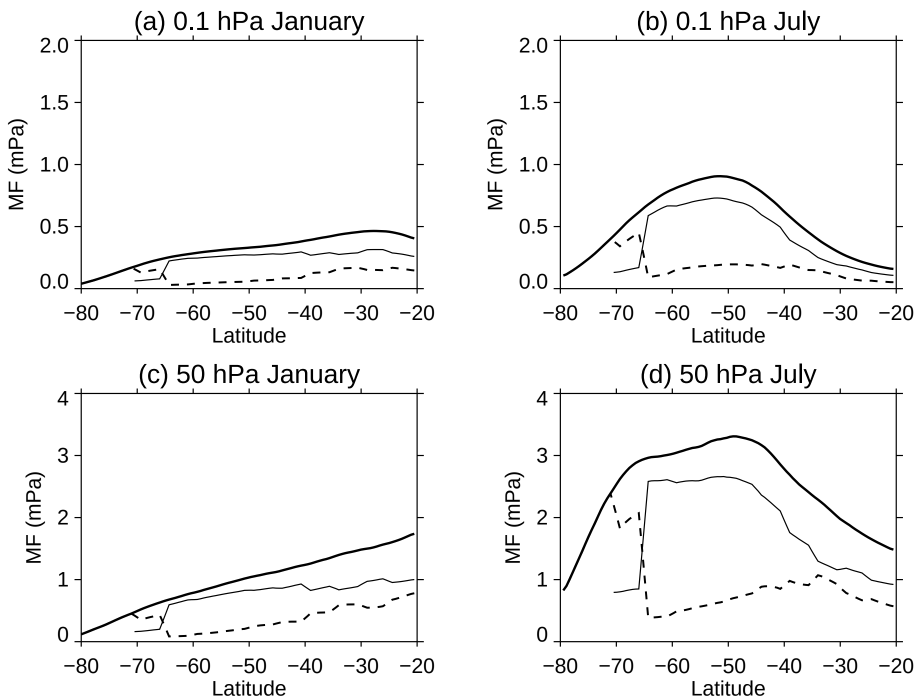

FIG. 8. January and July zonal-mean MF for the land (dashed) and oceanic (thin solid) regions at (a,b) 0.1 hPa and (c,d) 50 hPa. The thick solid line is the total MF. Note the different scales between the 50 hPa and 0.1 hPa pressure levels.

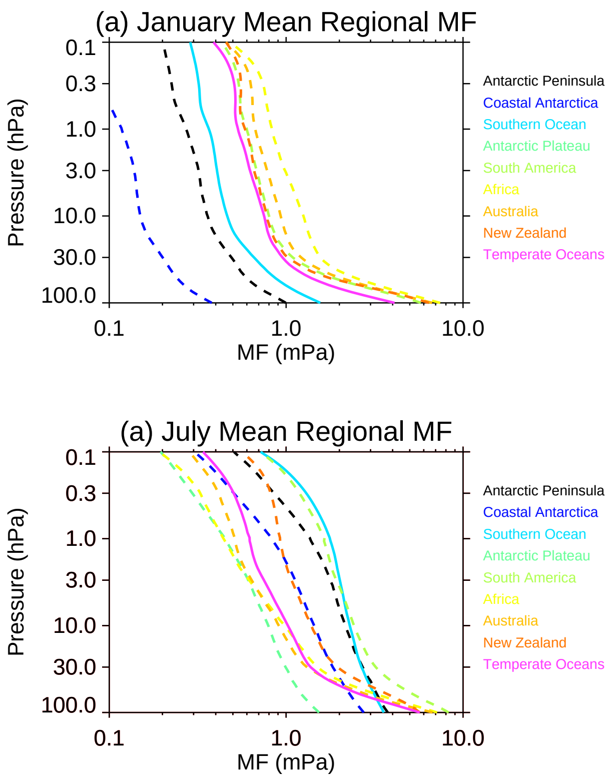

FIG. 9. Mean MF as a function of pressure level for each region for (a) January and (b) July. Solid lines indicate oceanic regions, while dashed lines indicate land regions.

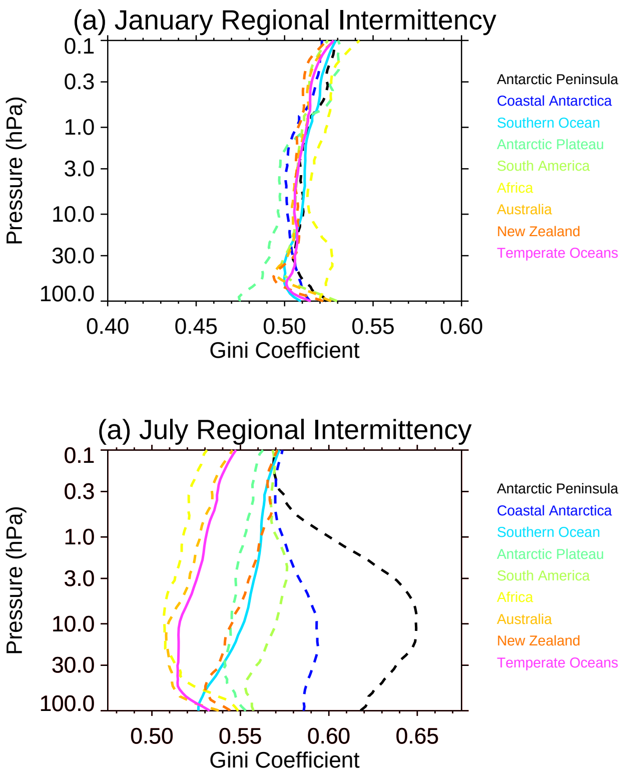

FIG. 10. Mean intermittency (as measured by the Gini coefficient) as a function of pressure level for each region for (a) January and (b) July. Solid lines indicate oceanic regions, while dashed lines indicate land regions.

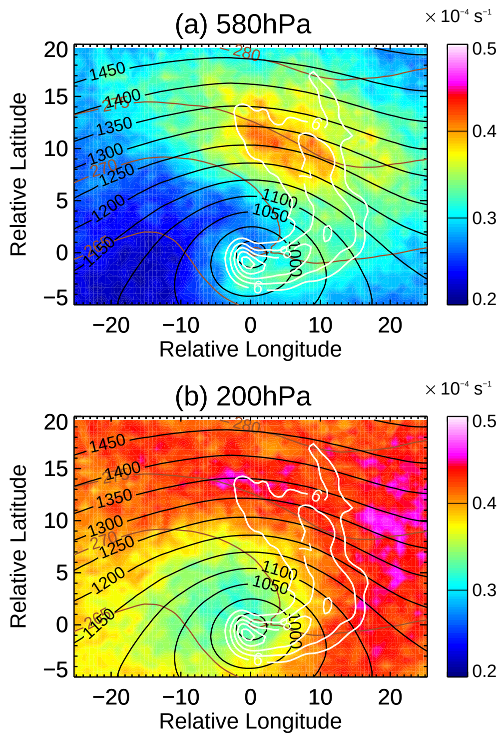

Fig. 11. (a) The July mean 580 hPa root mean square horizontal wind divergence (color contours) relative to the center of deep depressions above the ocean, along with the precipitation (white lines, mm day^{-1}), 850 hPa potential temperature in Kelvin (brown lines) and 850 hPa geopotential height in meters (black lines). (b) The same except showing the July mean 200 hPa root mean square horizontal wind divergence (color contours).

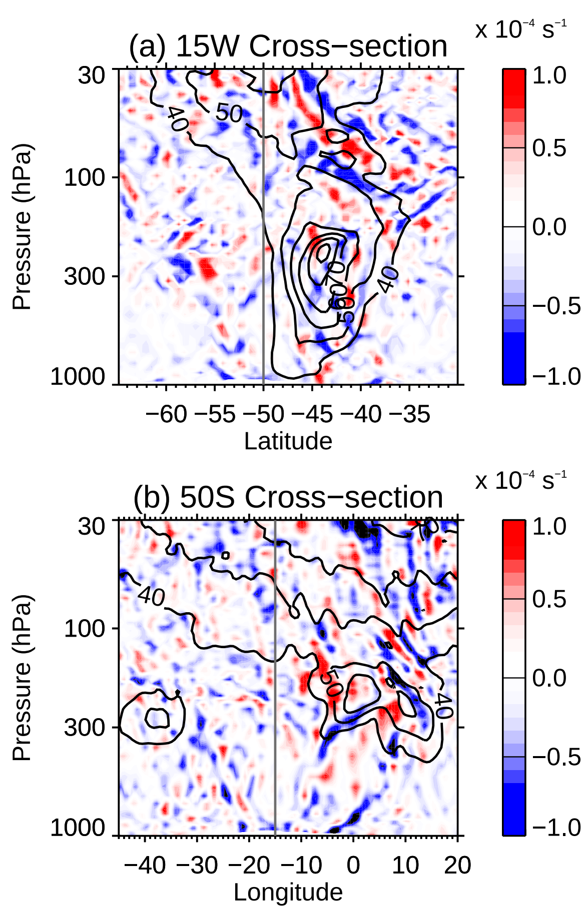

FIG. 12. Cross-sections in the South Atlantic of the horizontal wind divergence (color) and zonal wind (black lines, units of m s^{-1}) through the center of a depression at (a) 15°W and (b) 50°S. Vertical gray lines indicate the cross-section for each other's panel.

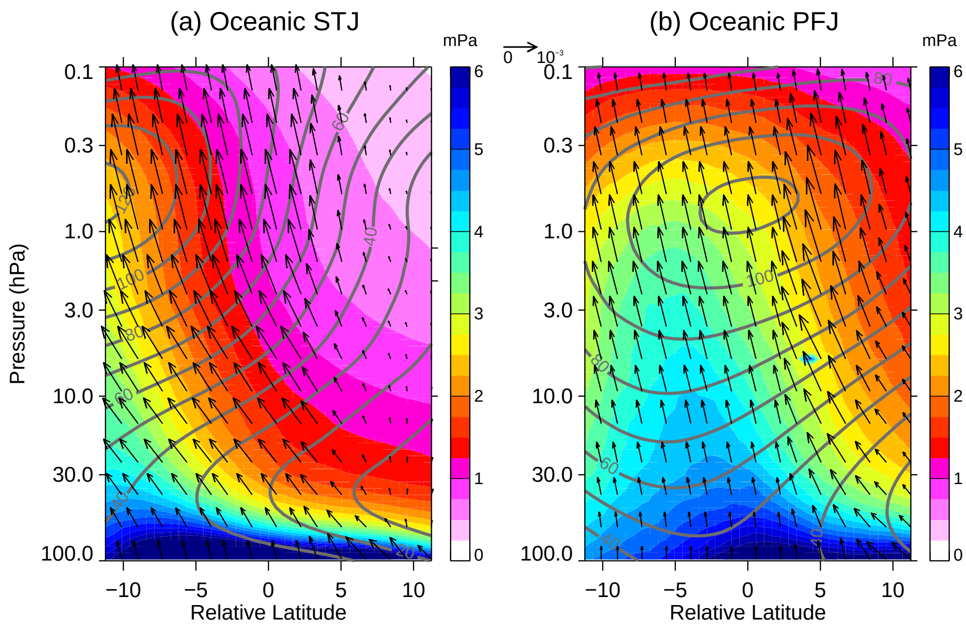

Fig. 13. July composite MF (color contours) and zonal wind (m s^{-1}, grey lines) for (a) STJ in the temperate oceans and (b) PFJ in the Southern Ocean. Vectors indicate the meridional and vertical wave potential energy flux ($\rho_0\overline{\phi' v'}$, $\rho_0\overline{\phi' w'}$). Vector lengths are constant between sub-panels with the magnitude given by the horizontal vector in the middle (units of kg m^{-1} s^{-2}). The $\rho_0\overline{\phi' w'}$ are multiplied by a factor of 20 for clarity.